CHEMISTRY OF MATERIALS

Article

pubs.acs.org/cm

Photothermal Plasmonic Triggering of Au Nanoparticle Surface Radical Polymerization

Joan M. Walker, Linfeng Gou, Sibaprasad Bhattacharyya, Sarah E. Lindahl, and Jeffrey M. Zaleski*

Department of Chemistry, Indiana University, Bloomington, Indiana 47405, United States

Supporting Information

ABSTRACT: Gold nanoparticle theranostic agents have dramatic potential in the fight against disease, particularly cancer, as multifunctional platforms combining biocompatibility, unique optical properties for detection/activation, and heat generation. In this vein, a new thiol-functionalized enediyne surfactant ligand was synthesized and coordinated to gold nanoparticles, as confirmed by the red-shift in the optical spectrum from λ = 520 to 529 nm upon ligand exchange. Raman spectra of the nanoparticle conjugate material show characteristic vibrations at 2192 (alkyne), 1582 (alkene), and 670 cm^{-1} (C−S). The photoreactivity of the material is explored under two sets of photolysis conditions: solution, λ_{exc} = 514 nm, RT, t = 8 h; solid aggregate, λ_{exc} = 785 nm, T = −190 °C, t = 4 h. Under these conditions, exciting into the surface plasmon of the Au nanoparticle substrate transfers heat to the organic ligand layer, initiating enediyne cyclization and generating surface radicals that lead to subsequent polymerization. New vibrational signatures arise in the alkyne (2170−1900 cm^{-1}) and aromatic (1520−1200 cm^{-1}) spectral regions, indicating the formation of highly conjugated species in the initial stages of the photoreaction. Prolonged irradiation results in the observation of a dense polymer coating in the TEM images, complete loss of observable molecular vibrations in the Raman spectra as a result of strong fluorescence, and a red-shift and broadening of the surface plasmon band in the electronic spectrum. Translation of this approach to nanorods and other architectures is also possible with carbon coatings clearly visible by TEM. The reported nanomaterial design represents a new approach to developing reactive biomedical agents for phototherapy applications, as well as a novel method toward carbonaceous coatings of nanoarchitectures.

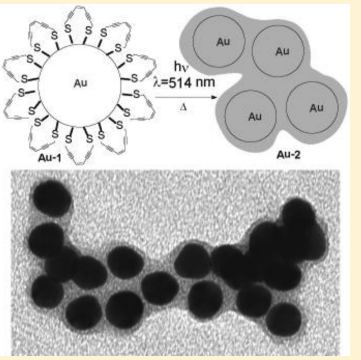

KEYWORDS: *(Au nanoparticles, surface functionalization, photothermal activation, radical polymerization)*

The development of theranostic (combined therapy and diagnostic) and multifunctional biomedical nanomaterials lies at the forefront of nanomedicine research, especially in the area of oncology.[1,2] To date, many architectural strategies have focused on employing established targeting modalities with well-known anticancer agents to affect therapeutic response. In these cases, the nanomaterial platform acts solely as a vehicle for drug targeting and delivery, which is then susceptible to the release of the chemotherapeutic agents via hydrolysis or passive diffusion upon reaching the target.[3−5] Although in some cases luminescence from the nanoparticle does provide detection and tracking information, the nanoscale platform is generally an inert spectator in the overall process and reactivity of the drug. Under these conditions, the surface functionalization solely modulates nanoparticle pharmacokinetics.[6,7]

Gold is particularly attractive as the basis for multifunctional nanomedicine agents because of its amenable surface chemistry, biocompatibility, and unique properties derived from the surface plasmon.[8−10] As passive or targeted drug delivery agents, the optical scattering behavior of gold nanoparticles, nanorods, and nanoshells allows them to be easily tracked *in vivo*. Beyond tracking, the past several years has seen increasing interest in the heat generation capabilities at the metal surface, wherein absorbed photons are quickly and efficiently transferred into thermal energy through plasmon−phonon coupling, etc.[11] Harnessing this heat has led to the development of photothermal therapies (hyperthermia) for cancer treatment,[12,13] as well as laser ablation as a means of malignant cell destruction.[14] More recently, plasmonic heating has been used to promote drug release through polymer phase change,[15] hybrid DNA cleavage,[16] or enhanced diffusion.[17] From these examples, it is clear that exciting possibilities exist for the continued progression of nanoplatforms as active participants in biomedical applications.

Our efforts have focused on developing a drug-mimicking, reactive, nanoplatform surface functionality and recruiting the inherent plasmon resonance of the nanomaterial to initiate particle surface reaction to control therapeutic activity. This concept is born out of the established antitumor properties of enediyne-containing natural products and their ability to be photoelectronically activated on demand to produce the same toxic 1,4-phenyl diradical intermediate as the basal thermal reaction. In fact, our group has developed a series of metal−enediyne small molecules (metalloenediynes) that, upon complexation of the enediyne ligand, can be thermally,[18] photoelectronically,[19] or photothermally[20] activated to form the purported 1,4-diradical intermediate capable of thermodynami-

Received: September 13, 2011
Published: November 10, 2011

cally favorable double H-atom abstraction from biological C−H bonds. These complexes serve as a chemical intermediary between the organic enediyne natural products and enediyne-coated nanomaterials for nanomedicine. In principle, the ability to photothermally activate such a surface functionality on a chromophoric, nanoscale platform could be the basis for an effective theranostic nanomedicine agent. Within this theme, we report the preparation of enediyne-coated Au-nano-conjugates and their surface plasmon resonance photothermal activation in both solid and solution states to yield surface diradical reactivity, the progress of which is tracked by both optical and Raman spectroscopy.

EXPERIMENTAL SECTION

Materials and Physical Measurements. All chemicals and solvents used were of the highest purity available from Aldrich and Alfa Aesar. Air-sensitive reactions were carried out under nitrogen using Schlenk techniques, and air-sensitive compounds were handled in an inert atmosphere drybox under N_2. ^{1}H NMR and ^{13}C NMR spectra were collected on a 400 MHz Varian Inova NMR spectrometer using the residual proton resonance of the solvent as an internal reference. Differential scanning calorimetry (DSC) measurements were made on a TGA Q10 DSC system with a TA Instruments thermal analyzer at a heating rate of 10 °C min^{-1}. High-resolution mass spectrometry (HRMS) was acquired on a Thermo MAT 95XP-Trap mass spectrometer with trace gas chromatograph. Optical spectra were collected on a Perkin-Elmer Lambda 19 spectrometer. Dynamic light scattering (DLS) was performed on a Zetasizer Nano-ZS fitted with a 633 nm laser, using a sample dilution of 50 μL Au colloid with 1 mL ethanol. Transmission electron microscopy (TEM) was performed on a JEOL 1010 instrument operating at 80 kV on samples prepared by dropcasting the alcohol solution onto Formvar-coated 300-mesh Cu grids. Samples were prepared for Raman analysis by drying a drop of the alcohol solution onto an aluminum-covered microscope slide. Spectra were collected on a Renishaw 1000B micro-Raman instrument using a λ_{exc} = 785 nm excitation wavelength, equipped with a Linkam Sci THMS 600 variable temperature stage, TMS 93 controller, and LNP liquid nitrogen pump. Raman spectra were analyzed using the GramsAI software package.

Synthesis of (*Z*)-oct-4-en-2,6-Diyn-1,8-Dithiol (1). 1,8-Dibromooct-4-en-2,6-diyne was synthesized following previously reported procedures.[21] To 1 equiv of dibromo was added 2.5 equiv of potassium thioacetate in dry THF. This mixture was stirred for 10−12 h under N_2 at 15−20 °C. The mixture was poured into water and then extracted with CH_2Cl_2. The organic phase was washed with water and then concentrated to obtain the crude product, which was purified using silica gel column chromatography (hexanes/ethyl acetate) in 65% yield. A solution of this product (1 equiv) in diethyl ether was added dropwise to a cold (−30 °C) stirring suspension of $LiAlH_4$ (1 equiv) in anhydrous diethyl ether. The reaction flask was stirred for 30 min. Excess hydride was quenched by the dropwise addition of aqueous NH_4Cl. The mixture was diluted with anhydrous CH_2Cl_2 and dried over Na_2SO_4. Product concentration for subsequent nanoparticle conjugate preparation was determined using ^{1}H NMR spectroscopy. ^{1}H NMR (400 MHz, 298 K, $CDCl_3$): δ (ppm) 5.82 (s, 2H), 3.27 (s, 4H), 2.09 (s, 2H). ^{13}C{^{1}H} NMR (400 MHz, 298 K, CD_2Cl_2): δ (ppm) 119.89 (CH), 95.72 (Cquat), 80.16 (Cquat), 18.64 (CH_2). HRMS (EI), m/z: 168.0067 (M^+) [HRMS calcd for $C_8H_8S_2$: 168.0062].

Synthesis of Gold Nanoparticle Colloid (Au−Citrate). Following the classic citrate reduction method pioneered by Turkevich et al., a stable aqueous colloid of 20 nm Au nanoparticles was prepared.[24] Briefly, 1 mL of a 1% w/w solution of $HAuCl_4 \cdot 3H_2O$ was added to 100 mL H_2O and brought to a boil. Upon boiling, 3 mL of a 1% w/w trisodium citrate dihydrate solution was added. The mixture immediately turned colorless, blue, and finally pink, indicating the formation of metallic gold nanoparticles. Boiling was continued for 15 min. This stock solution was removed from heat and used for all subsequent procedures.

Preparation of Au−1 nanoparticle conjugates. Au−ligand conjugates were prepared by facile ligand place exchange of the Au−citrate with **1** in ethanolic solution. Au−citrate (1.5 mL) was centrifuged, and the colorless-to-slightly pink supernatant was removed with a syringe. Ethanol (1 mL) was added to the centrifuge tube and the mixture was sonicated for 15 min to produce a red colloid. Care must be taken during this solvent transfer step (avoiding excessive centrifugation, for example) to prevent forming a blue−purple colloid, which indicates aggregation of the Au nanoparticles in the alcohol. A solution of **1** was prepared separately by diluting 50 μL of the stock **1** solution (1.06 mM) with 0.5 mL ethanol. This solution was added to the Au colloid in the centrifuge tube, which was subsequently wrapped with aluminum foil and left undisturbed overnight. After ligand exchange, the sample was either used directly for the photolysis experiments or physically aggregated by centrifugation (8000 rpm, 20 min) for solid phase experiments.

Solution Photolysis. The 1 mL samples were transferred into 1 cm square quartz cuvettes along with a small magnetic stirbar and capped with a septum. The temperature in the solution was monitored using a K-type microthermocouple (Omega Engineering, Inc.) threaded through the septum cap. Samples were irradiated with the λ_{exc} = 514 nm line of a Coherent Innova Ar ion laser. Laser power was measured to be 250 mW at the sample with an 8 mm beam diameter.

Solid Photolysis. Samples were prepared by dropcasting Au−**1** or Au−**1** aggregate colloids onto aluminum covered slides and allowing solvent to evaporate in the dark. For Au−**1**, the dried sample was irradiated at λ = 514 nm (400 mW, 8 mm spot size). For Au−**1** aggregate, the samples were directly irradiated in the micro-Raman instrument at λ_{exc} = 785 nm (0.2 − 20 mW, 1 mm spot size).

Preparation of Au−1 Nanorod Conjugates. Short Au nanorods were prepared according to the method of Nikoobakht and El-Sayed.[38] Ligand place exchange with **1** was achieved following a similar route as for the Au nanoparticles. Samples for photolysis were deposited onto an aluminum substrate for irradiation at λ_{exc} = 785 nm at room temperature and were subsequently redispersed into ethanol with sonication.

RESULTS AND DISCUSSION

In our interest to create a gold nanoparticle conjugate with radical generating properties, a new thiol-functionalized enediyne ligand (**1**) was developed[21,22] in order to take advantage of the strong sulfur-to-noble metal association. The 1,8-dibromo enediyne starting material[21] reacts with 2.5 equiv of potassium thioacetate in dry THF to yield the thioacetate precursor in 65% (Scheme 1). Deprotection to the free dithiol

Scheme 1. Synthesis of (*Z*)-octa-4-en-2,6-Diyne-1,8-Dithiol (1) from Known 1,8-Dibromo Analogue

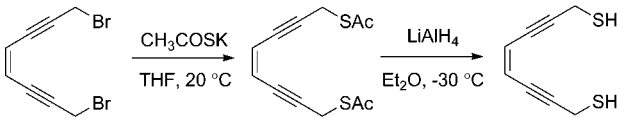

1

was accomplished by dropwise addition of 1 equiv to a cold (−30 °C) stirring suspension of $LiAlH_4$ in anhydrous diethyl ether (30 min) and dropwise addition of aqueous NH_4Cl to quench excess hydride. Product concentration for subsequent nanoparticle conjugate preparation was determined by ^{1}H NMR spectroscopy. In its pure form, **1** is colorless, photostable, and nonabsorbing at all visible excitation wavelengths used in the photolysis experiments. However, it is thermally unstable as a neat oil and exhibits a broad, exothermic maximum centered at 150 °C in the differential scanning calorimetry (Figure S1 in

dx.doi.org/10.1021/cm202741p | *Chem. Mater.* 2011, 23, 5275−5281

Scheme 2. Au−1 Conjugate Preparation from Citrate-Stabilized Nanoparticles via Ligand Exchange[a]

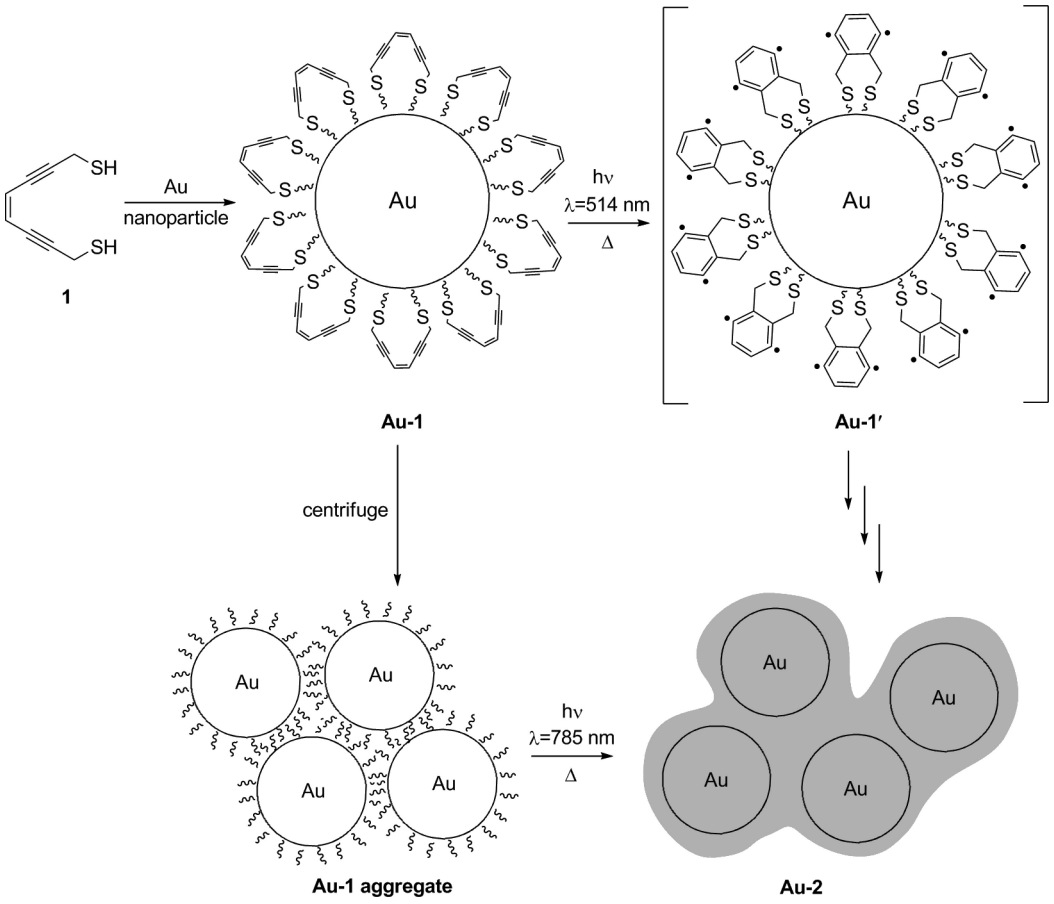

[a]Heating or irradiating this material induces Bergman-type cyclization (Au−**1**′), leading to a polymerized coating (Au−**2**). Alternatively, Au−**1** can be physically aggregated (Au−**1** aggregate), which shortens the average interparticle distance and alters the optical properties.

the Supporting Information) characteristic of the cyclization of small enediyne ligands.[23] The moderate thermal barrier of **1** to cyclization suggests that it may be a viable candidate for forming stable, yet photothermally reactive nanoparticle−enediyne conjugates.

Gold nanoparticles used for conjugation were synthesized via the citrate reduction method[24] and transferred into ethanol for ligand exchange with **1** to form a stable colloid (Au−**1**, Scheme 2). Excess dithiol surfactant was removed by simple centrifugation (10 min, 7000 rpm), while longer centrifugation times at higher speeds (20 min, 8000 rpm) leads to particle aggregation (Au−**1** aggregate), which drastically shortens their average interparticle distance and enhances particle−particle electronic communication. Photolysis in ethanolic solution (at λ_{exc} = 514 nm) or dried aggregated (λ_{exc} = 785 nm) and subsequent Raman analysis (λ_{exc} = 785 nm) was used to monitor the photothermally induced cyclization of the surfactant ligand.

Coordination of **1** to the gold surface is confirmed by Raman spectroscopy (Figure 1). The pure ligand spectrum reveals sharp, readily assignable vibrations of the key functional groups within the ligand framework (Table 1), most notable of which are ν(S−H) at 2563 cm^{-1} and the strong alkyne stretches at 2211 and 2194 cm^{-1}.[25]

In the particle conjugate spectrum, an overall broadening and slight shift to lower frequency are observed, indicating that a variety of conformations are present and a strong interaction

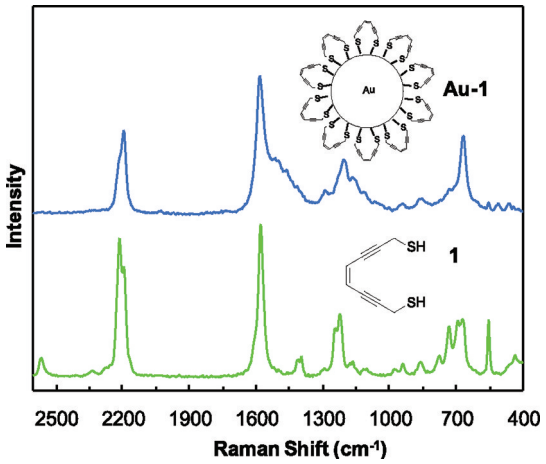

Figure 1. Raman spectra of **1** and Au−**1** after 12 h ligand exchange. Although broadened, the spectrum of Au−**1** clearly exhibits strong alkyne (2192 cm^{-1}), alkene (1582 cm^{-1}), and C−S (670 cm^{-1}) vibrations. The absence of thiol S−H stretch at 2563 cm^{-1} indicates the covalent coordination of **1** to the metal surface.

between the ligand and surface exists.[26] Clearly identifiable spectral features are present in the Au−**1** spectrum, including the alkyne, alkene, and C−S stretches. Importantly, there is no evidence for the thiol S−H stretch at 2563 cm^{-1}, indicating that there is indeed surface coordination to the particle through the

dx.doi.org/10.1021/cm202741p | *Chem. Mater.* 2011, 23, 5275−5281

Table 1. Assignment of Vibrations in Raman Spectrum of 1

frequency (cm^{-1})	assignment
2563	ν(S−H)
2211, 2194	ν(C≡C)
1579	ν(C=C)
1414, 1397	$\delta(CH_2)$
1244, 1223	CH sym rock, CH_2 wag
941, 734	δ(CH) out-of-plane
692, 673	ν(C−S)
556	C=C skeletal

thiol sulfur. Because of the instability of the materials, it is important to note that Raman spectra of the free ligand were collected with a freshly prepared, neat sample. Similarly, all calibration Raman spectra of the pure nanoparticle conjugate material were collected at low temperature (−190 °C) to minimize photoinduced thermal effects on the samples.

The optical spectra of the nanoparticle samples (Figure 2) exhibit the characteristic λ = 520 nm absorbance of Au−citrate,

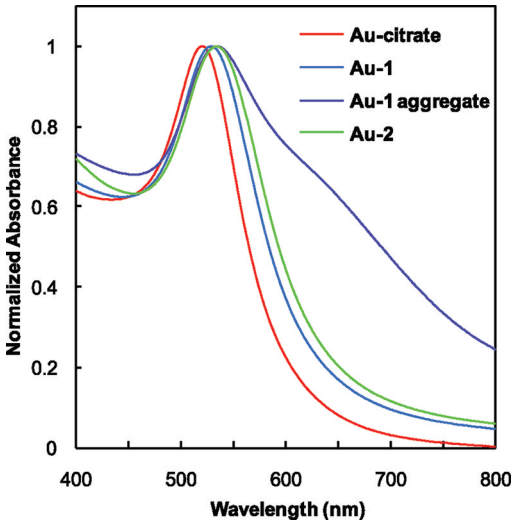

Figure 2. Nanoparticle optical spectra showing the change in surface plasmon resonance with alterations at the Au surface. The absorbance maximum shifts from 520 to 529 nm upon ligand exchange (Au−citrate and Au−**1**). Upon photolysis for 8 h (λ_{exc} = 514 nm), the maximum further shifts to 535 nm (Au−**2**). Centrifugation-mediated aggregation of Au−**1** red-shifts the peak maximum to 534 nm and increases long wavelength absorbance in the region between 600 and 800 nm.

which shifts to λ = 529 nm upon ligand exchange as a result of the change in surface coordination for Au−**1**. Au−**1** aggregate exhibits a further red shift in the absorbance maximum to λ = 534 nm and increased long wavelength absorbance as a result of communication between individual particles.[27] Upon photolysis of Au−**1** (8 h, λ = 514 nm), the absorbance maximum shifts to λ = 535 nm and broadens slightly, indicative of reaction at the particle surface to form Au−**2** (*vide infra*); however, the samples still behave as stable sols. Dynamic light scattering analysis echoes the sol behavior suggested from the optical spectra (Figure S2, Supporting Information). These are in comparison to Au−citrate, which exhibits a single, narrow peak typical of monodisperse, nonaggregated sols. Ligand exchange increases the size of the solvation shell for Au−**1**, and a new population of widely polydisperse aggregates appears.

The solution behavior of the gold nanoparticles is paralleled in the dried TEM samples, images of which reveal spherical particles of size 17 ± 1.5 nm (Figure 3a). Au−**1** dries into small

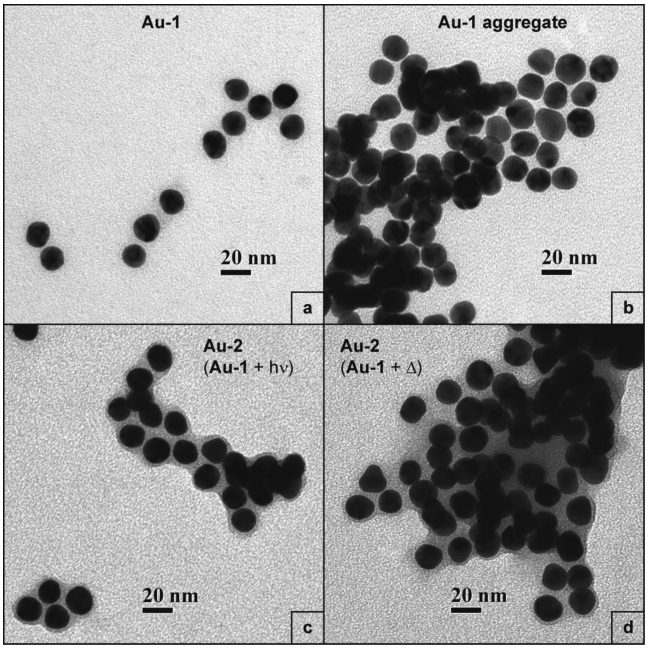

Figure 3. TEM images reveal spherical Au nanoparticles of diameter 17 ± 1.5 nm. (a) They are well-dispersed in the ligand stabilized sample but (b) can be physically aggregated by centrifugation, which shortens the interparticle distance to <1 nm and modulates their electronic properties. For solution samples, a thick polymer coating forms after either (c) photolysis at λ_{exc} = 514 nm or (d) direct heating at 50 °C for 8 h.

clumps of a few particles because interactions between adjacent surfaces draw them together as the solvent evaporates after deposition. In contrast, large aggregates are formed upon centrifugation (Figure 3b, Au−**1** aggregate), consistent with the broadening and redshift in the optical spectra of the material. Irradiation of Au−**1** at λ_{exc} = 514 nm (Figure 3c) or heating (Figure 3d) at 50 °C for 8 h leads to a dense surface coating of the particles, indicating surface enediyne reactivity under these conditions. The polymer coating is consistent with radical generation subsequent to enediyne cyclization, which in the high density surface environment, leads to radical−radical and radical-multiple bond coupling.[20]

The photocyclization and subsequent polymerization events can also be monitored via the Raman (λ_{exc} = 785 nm) spectra of Au−**1** and Au−**1** aggregate as a function of in-resonance (Au−**1**, λ_{exc} = 514 nm; Au−**1** aggregate, λ_{exc} = 785 nm) irradiation time (Figure 4a and b). Spectral variations of note include the decay of the discrete alkyne (2192 cm^{-1}) and vinylic (1582 cm^{-1}) vibrations and simultaneous growth of new features in the aromatic region (1200−1500 cm^{-1}), indicating conversion of the enediyne molecules to highly conjugated extended aromatic structures. Additionally, continued photo-irradiation leads to significant increase in the fluorescent background, which is consistent with polymer formation.[20] Together, these spectral changes reflect transformation of the surface ligands into multiple polymeric substructures on the nanoparticle.

In situ photoconversion is also observable in the Raman experiment directly, but the reactivity is dependent upon

dx.doi.org/10.1021/cm202741p | *Chem. Mater.* 2011, 23, 5275–5281

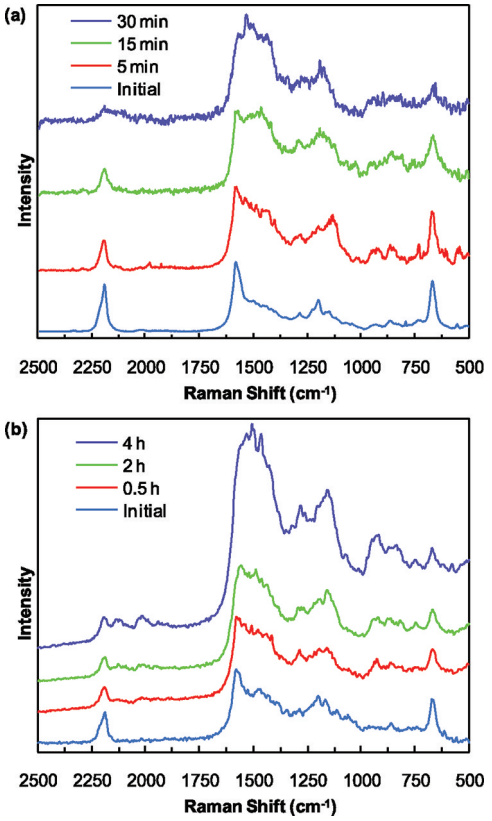

Figure 4. (a) Raman spectra of Au−**1** after photolysis at λ_{exc} = 514 nm (400 mW) at room temperature. (b) Raman spectra of Au−**1** aggregate after photolysis at λ_{exc} = 785 nm (20 mW) at −190 °C. No further change is observed after 4 h for Au−**1** aggregate, while the spectra for Au−**1** become featureless after 30 min. Similar spectral changes can be noted in both, particularly in the shape of the alkyne region and the shift in the conjugated C═C area (1500 − 1600 cm^{-1}), corresponding to the decay of the vinylic peak of the enediyne and growth of aromatic ring structures. All spectra were collected at 2 mW over 60 s, and spectral traces have been baseline corrected and offset for clarity.

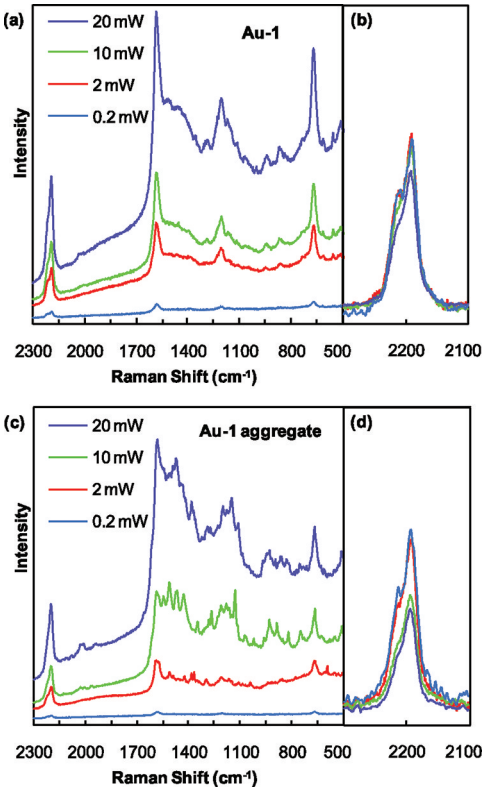

Figure 5. (a) Raman spectra of Au−**1** as a function of off-resonance excitation power reveal photostability toward λ_{exc} = 785 nm irradiation up to 20 mW with (b) the alkyne region exhibiting very little decay of the 2192 cm^{-1} vibration. (c) In contrast, Raman spectra of Au−**1** aggregate in resonance with the long wavelength absorption (λ_{exc} = 785 nm) indicate photochemical conversion of the Au surface coating, as evidenced by the appearance of new spectral features and (d) loss of alkyne vibration intensity.

resonance between the Raman excitation wavelength and the nanoparticle plasmon, which is specifically determined by the degree of aggregation of the sample (Figure 5a and b). Nonaggregated Au−**1** with λ_{max} at 529 nm is stable to λ_{exc} = 785 nm excitation (Figure 5a), except at the very highest laser power (20 mW). In contrast, Au−**1** aggregate reacts at much lower laser powers, even at very low temperature, as a result of the increased absorptivity of the aggregate at 785 nm. Steady decline in the intensity of the alkyne stretch suggests that the enediyne unit undergoes cyclization type reactivity involving transformation of the triple bonds to generate multiple radical species. The fact that the Raman peak at 2192 cm^{-1} is never entirely extinguished is attributable to the preservation of some of the triple bonded species in unreacted or partially reacted and deactivated molecules.

Because the behavior of the nanomaterial is dependent on the degree of aggregation of the sample, it is clear that the observed reactivity is due to nonradiative decay upon plasmonic excitation and not traditional vibrational laser heating. As seen in the optical and electron microscopy data, the important difference between Au−**1** and Au−**1** aggregate is the interparticle distance, which leads to electronic communication between sites and, therefore, increased absorbance at the Raman excitation wavelength (λ_{exc} = 785 nm). This interparticle coupling also sharpens the Raman spectra of molecules located between individual particles sites, which is most noticeable in the spectra collected at higher powers.[27] Subtraction of the fluorescent background further highlights the developing vibrational features (Figure 6a and b). Prominent new vibrations in the aromatic region attest to the formation of highly conjugated polymeric species in the initial stages of the photoreaction. Many of the new Raman vibrations (Figure 6b) arise at frequencies typical for C−C, C═C, and combinations of C═C and C−H vibrations of polyaromatic hydrocarbons such as pyrene, perylene, and oligofluorene.[28−30] Moreover, the 1,2-benzenedimethanethiol cyclized product analogue of Au−**1′**, which is stable to extended irradiation, also exhibits features at similar frequencies (Figure S3, Supporting Information). Thus, plasmonic excitation of Au−**1** aggregate at λ_{exc} = 785 nm definitively leads to radical cyclization of the surface ligand.

In addition to monitoring photocyclization of solid state material, extended irradiation of solution samples or external heating leads to the same increase in fluorescence in the Raman spectra (Figure 7a and b). Irradiation of solution samples in plasmonic resonance at λ_{exc} = 514 nm heats the nanoparticles, as evidenced by an increase in the bulk solution temperature of ∼5 °C over 4 h as a result of absorption and nonradiative decay. Although the bulk temperature jump seems inconsequential, the actual surface temperature of the gold nanoparticle is likely markedly higher[31] and is sufficient to trigger the surface

dx.doi.org/10.1021/cm202741p | *Chem. Mater.* 2011, 23, 5275−5281

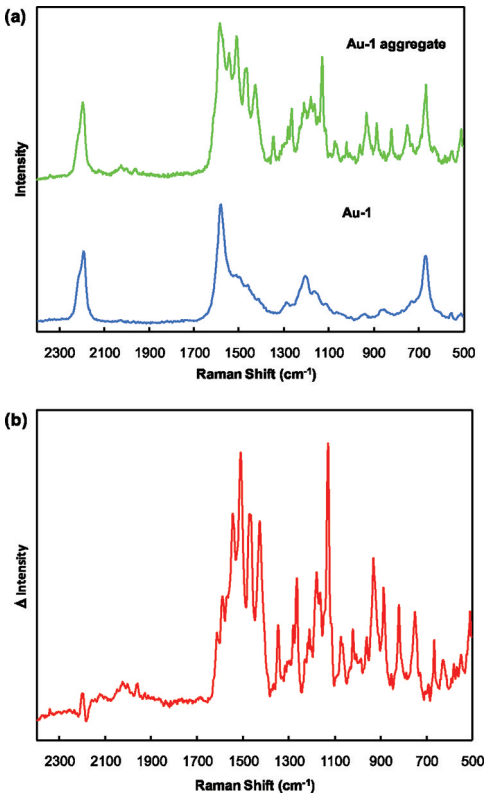

Figure 6. (a) Corrected Raman profile for the photolyzed Au−**1** aggregate in relation to the initial spectrum for Au−**1** and (b) the resulting difference spectrum. Baseline correcting for the fluorescent polymer background in the Au−**1** aggregate trace reveals sharp features, indicating the creation of new highly conjugated species, as well as unreacted Au−**1** surface coating (ν = 2192 cm^{-1}). Subtracting out the unreacted component of the photolyzed spectrum highlights the new vibrations. While the identities of the new constituents in the coating are at present unknown, their vibrational spectra share some resemblance to those of oligofluorenes and polyaromatic hydrocarbons.

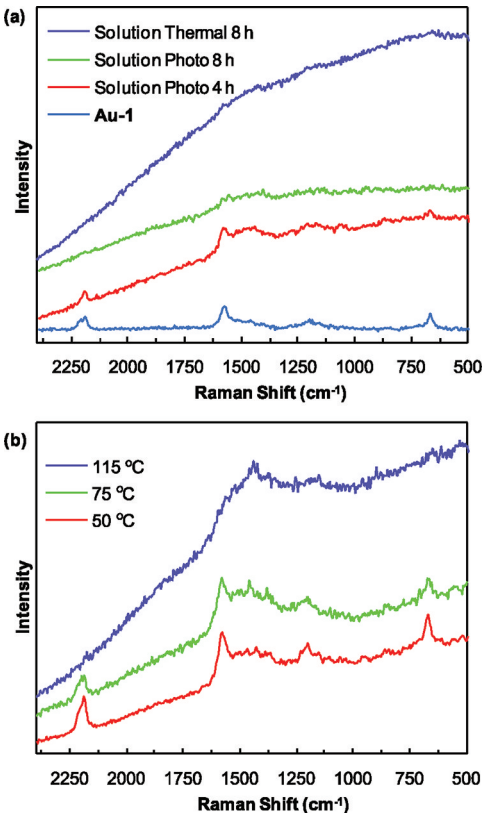

Figure 7. Raman spectra (λ_{exc} = 785 nm) depicting the photochemical and temperature-dependent conversion of the Au−**1** surface coating. (a) Samples prepared after 4 and 8 h of photolysis (λ_{exc} = 514 nm) in solution show a decay of discrete vibrations of the ligand and increase in fluorescence background, consistent with polymer formation at the nanoparticle surface. Similar behavior is observed for solution samples heated at 50 °C. (b) Thermal activation of dried samples also promotes temperature-dependent surface molecule polymerization. Samples were dried on foil-covered slides and heated to 50, 75, or 115 °C in an oven for 20 min. Raman spectra were collected for all samples at −190 °C and 0.2 mW, and the selected traces have been offset slightly for clarity.

molecule cyclization giving rise to increased fluorescence in the Raman spectra. Similarly, external heating of the solution or dried samples in an oven in excess of 50 °C induces polymer formation similar to that seen as a result of extended photoirradiation, as evidenced by enhanced fluorescence in the Raman spectrum and the thick polymer coating visible in TEM images seen in Figure 3.

Finally, other gold nanostructures, such as rods, can also be coated with **1** and photochemically or thermally activated analogously to the gold spheres to polymer coat other nanoarchitectures (Figure 8). The controlled polymer formation on the surface of the nanostructures has potentially interesting applications for developing networks of particles within a scaffold.[32] Additionally, the optical properties exhibited by gold nanorods and other particle morphologies show increased absorbance in the near-infrared region, which is important for biomedical applications such as photodynamic therapy in light of wavelength-dependent tissue transparency. Moreover, the polymer coating can be subsequently pyrolyzed to form a solid disordered graphite surface layer.[33] A thin carbon coating is known to enhance the thermal[34,35] and chemical stability[36] of many nanoparticles, and in the case of silver, may even increase SERS signals.[37] Therefore, the development of such coatings could significantly impact biomedical and materials applications.

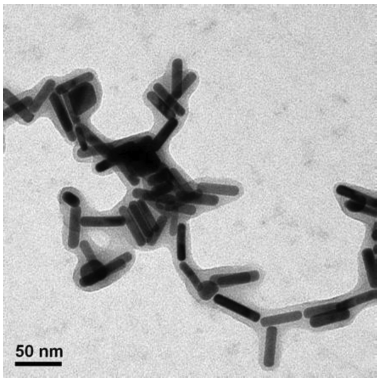

Figure 8. TEM image of photopolymerized Au nanorod−**1** conjugates irradiated with λ_{exc} = 785 nm at room temperature for 12 h.

CONCLUSION

The chemical synergy of gold nanoparticle surface plasmon resonance and thermally reactive, thiol-substituted enediyne

dx.doi.org/10.1021/cm202741p | *Chem. Mater.* 2011, 23, 5275–5281

surface functionality allows for the development of reactive, radical-generating nanoarchitectures that form networks of polymer-coated particles upon photothermal activation and nonradiative decay. Evidence for radical-mediated polymerization derives from electronic spectral redshifts and Raman vibrational signature transformations as a function of photolysis time and/or thermal heating both in solid and solution samples. Decrease in the intensity of the alkyne (2192 cm^{-1}) and vinylic (1582 cm^{-1}) vibrations, with concomitant growth of new features in the aromatic region (1200−1500 cm^{-1}) typical for C−C, C═C, and combination vibrations of polyaromatic hydrocarbons such as pyrene, perylene, and oligofluorene. TEM images verify the vibrational predictions that the nanoarchitectures are indeed encapsulated within a carbonaceous coating that can be annealed at high temperatures to yield a uniform carbon coating. The design and realization of such coatings has significant potential for initiating rapid and high density radical formation for biomedical applications, as well as instantaneous particle property changes or customized coatings for materials development.

■ ASSOCIATED CONTENT

Supporting Information

DSC trace of **1**, DLS analysis of gold nanoparticles, and Raman spectra of 1,2-benzenedimethanethiol controls. This material is available free of charge via the Internet at http://pubs.acs.org.

■ AUTHOR INFORMATION

Corresponding Author

*E-mail: zaleski@indiana.edu.

■ ACKNOWLEDGMENTS

The generous support of the National Science Foundation (CHE-0956447), Walther Cancer Foundation, and Indiana University (FRSP) are gratefully acknowledged. J.M.W. thanks the Indiana University Graduate School Women in Science fellowship program.

■ REFERENCES

(1) Jelveh, S.; Chithrani, D. B. *Cancers* **2011**, *3* (1), 1081−1110.
(2) Xie, J.; Lee, S.; Chen, X. *Adv. Drug Delivery Rev.* **2010**, *62* (11), 1064−1079.
(3) Cheng, Y.; Meyers, J. D.; Broome, A.-M.; Kenney, M. E.; Basilion, J. P.; Burda, C. *J. Am. Chem. Soc.* **2011**, *133* (8), 2583−2591.
(4) Hwu, J. R.; Lin, Y. S.; Josephrajan, T.; Hsu, M.-H.; Cheng, F.-Y.; Yeh, C.-S.; Su, W.-C.; Shieh, D.-B. *J. Am. Chem. Soc.* **2009**, *131* (1), 66−68.
(5) Kim, D.; Jeong, Y. Y.; Jon, S. *ACS Nano* **2010**, *4* (7), 3589−3696.
(6) Khlebtsov, N.; Dykman, L. *Chem. Soc. Rev.* **2011**, *40* (3), 1647−1671.
(7) Perrault, S. D.; Walkey, C.; Jennings, T.; Fischer, H. C.; Chan, W. C. W. *Nano Lett.* **2009**, *9* (5), 1909−1915.
(8) Boisselier, E.; Astruc, D. *Chem. Soc. Rev.* **2009**, *38* (6), 1759−1782.
(9) Dreaden, E. C.; Mackey, M. A.; Huang, X.; Kang, B.; El-Sayed, M. A. *Chem. Soc. Rev.* **2011**, *40* (7), 3391−3404.
(10) Jain, P. K.; Huang, X.; El-Sayed, I. H.; El-Sayed, M. A. *Acc. Chem. Res.* **2008**, *41* (12), 1578−1586.
(11) Kyrsting, A.; Bendix, P. M.; Stamou, D. G.; Oddershede, L. B. *Nano Lett.* **2010**, *11* (2), 888−892.
(12) Nedyalkov, N. N.; Imamova, S. E.; Atanasov, P. A.; Toshkova, R. A.; Gardeva, E. G.; Yossifova, L. S.; Alexandrov, M. T.; Obara, M. *Appl. Surf. Sci.* **2011**, *257* (12), 5456−5459.
(13) Ungureanu, C.; Kroes, R.; Petersen, W.; Groothuis, T. A. M.; Ungureanu, F.; Janssen, H.; van Leeuwen, F. W. B.; Kooyman, R. P. H.; Manohar, S.; van Leeuwen, T. G. *Nano Lett.* **2011**, *11* (5), 1887−1894.
(14) Bartczak, D.; Muskens, O. L.; Millar, T. M.; Sanchez-Elsner, T.; Kanaras, A. G. *Nano Lett.* **2011**, *11* (3), 1358−1363.
(15) Zhao, X.-q.; Wang, T.-x.; Liu, W.; Wang, C.-d.; Wang, D.; Shang, T.; Shen, L.-h.; Ren, L. *J. Mater. Chem.* **2011**, *21* (20), 7240−7247.
(16) Dhar, S.; Daniel, W. L.; Giljohann, D. A.; Mirkin, C. A.; Lippard, S. J. *J. Am. Chem. Soc.* **2009**, *131* (41), 14652−14653.
(17) You, J.; Zhang, G.; Li, C. *ACS Nano* **2010**, *4* (2), 1033−1041.
(18) Bhattacharyya, S.; Pink, M.; Baik, M.-H.; Zaleski, J. M. *Angew. Chem., Int. Ed.* **2005**, *44* (4), 592−595.
(19) Benites, P. J.; Holmberg, R. C.; Rawat, D. S.; Kraft, B. J.; Klein, L. J.; Peters, D. G.; Thorp, H. H.; Zaleski, J. M. *J. Am. Chem. Soc.* **2003**, *125* (21), 6434−6446.
(20) Kraft, B. J.; Coalter, N. L.; Nath, M.; Clark, A. E.; Siedle, A. R.; Huffman, J. C.; Zaleski, J. M. *Inorg. Chem.* **2003**, *42* (5), 1663−1672.
(21) Benites, P. J.; Rawat, D. S.; Zaleski, J. M. *J. Am. Chem. Soc.* **2000**, *122* (30), 7208−7217.
(22) Castro, J.; Moyano, A.; Pericas, M. A.; Riera, A. *Synthesis* **1997**, No. 05, 518−520.
(23) Rawat, D. S.; Zaleski, J. M. *Chem. Commun.* **2000**, *24*, 2493−2494.
(24) Turkevich, J.; Stevenson, P. C.; Hillier, J. *Discuss. Faraday Soc.* **1951**, *11*, 55−75.
(25) Socrates, G. *Infrared and Raman Characteristic Group Frequencies: Tables and Charts*, 3rd ed.; Wiley: Chichester, New York, 2001.
(26) Lee, T. G.; Kim, K.; Kim, M. S. *J. Phys. Chem.* **1991**, *95* (24), 9950−9955.
(27) Ghosh, S. K.; Pal, T. *Chem. Rev.* **2007**, *107* (11), 4797−4862.
(28) Frank, O.; Jehlicka, J.; Edwards, H. G. M. *Spectrochim. Acta, Part A* **2007**, *68* (4), 1065−1069.
(29) Taylor, C. E.; Schoenfisch, M. H.; Pemberton, J. E. *Langmuir* **2000**, *16* (6), 2902−2906.
(30) Tsoi, W. C.; Lidzey, D. G. *J. Phys.: Condens. Matter* **2008**, *20* (12), 125213.
(31) Govorov, A. O.; Richardson, H. H. *Nano Today* **2007**, *2* (1), 30−38.
(32) Fernandes, R.; Li, M.; Dujardin, E.; Mann, S.; Kanaras, A. G. *Chem. Commun.* **2010**, *46* (40), 7602−7604.
(33) Yang, X.; Li, Z.; Zhi, J.; Ma, J.; Hu, A. *Langmuir* **2010**, *26* (13), 11244−11248.
(34) Khalavka, Y.; Ohm, C.; Sun, L.; Banhart, F.; Sonnichsen, C. *J. Phys. Chem. C* **2007**, *111* (35), 12886−12889.
(35) Ciuculescu, D.; Dumestre, F.; Comesana-Hermo, M.; Chaudret, B.; Spasova, M.; Farle, M.; Amiens, C. *Chem. Mater.* **2009**, *21* (17), 3987−3995.
(36) Galakhov, V. R.; Shkvarin, A. S.; Semenova, A. S.; Uimin, M. A.; Mysik, A. A.; Shchegoleva, N. N.; Yermakov, A. Y.; Kurmaev, E. Z. *J. Phys. Chem. C* **2010**, *114* (51), 22413−22416.
(37) Liu, F.; Cao, Z.; Tang, C.; Chen, L.; Wang, Z. *ACS Nano* **2010**, *4* (5), 2643−2648.
(38) Nikoobakht, B.; El-Sayed, M. A. *Chem. Mater.* **2003**, *15* (10), 1957−1962.